

# Influence of high power diode laser surface melting on the pitting corrosion resistance of type 316L stainless steel

C. CARBONI, P. PEYRE

*Coopération Laser Franco-Allemande (CLFA), 94112 Arcueil, France*

*E-mail: ppeyre@clfa.fr*

G. BÉRANGER, C. LEMAITRE

*Laboratoire Roberval, UPRESA du CNRS, 60205, Université de Technologie de Compiègne, France*

High Power Diode Lasers (HPDL) are becoming more and more attractive for industrial materials processing because of their high efficiency, low running costs, small sizes and low weight. Surface melting experiments have been carried out on 316L steel with a 1 kW HPDL, with application to modify its pitting corrosion resistance in NaCl 0.05 M. Surface modifications have been investigated with optical microscopy for the microstructure, microprobe analysis for the chemical content and X Ray Diffraction for phase transformations and residual stresses. Heat conduction characteristics, analysed with a 2D Finite element code, have driven to a 28% calculated absorption of the laser light generating nearly 400  $\mu\text{m}$  melted depth. A refinement and homogenization of structure together with  $\delta$ -ferrite transformation and the dissolution of inclusions was found in the melted thickness, driving to enhanced pitting resistance (nearly + 0.2 V on the pitting potential values, and factor 2 decrease of the passive current density). This pitting resistance, investigated at different depths below the surface, was found to be little affected by the  $\delta$  ferrite content (6% estimated value), and the fineness of the microstructure, but depreciated by the surface state without post-polishing. Therefore, it is believed that localized corrosion improvements can be mainly attributed to the dissolution of Al-base and Mn-base detrimental inclusions, despite the generation of up to 6%  $\delta$  ferrite susceptible to drive to enhanced galvanic couplings with  $\gamma$  phase. © 2002 Kluwer Academic Publishers

## 1. Introduction

Austenitic stainless steel are extensively used in nuclear power plants, or chemical industries, because of their mechanical properties and good corrosion resistance. However, localized corrosion attacks can occur in service. For instance, the presence of MnS inclusions which are active sites for pitting in 304 or 316-type steels, are known to depreciate the pitting corrosion resistance [1–3]. More, on sensitized zones, stainless steels exhibit a worse intergranular corrosion (IGC) resistance, due to the development of chromium-rich carbides along grain boundaries and chromium-depleted zones adjacent to these carbides.

Among all the treatments susceptible to modify the microstructure and improve the corrosion behavior, laser surface melting (LSM) appears to be an easy and rather inexpensive process for chemical and mechanical surface modifications. LSM homogenizes the microstructure and generates a grain and dendrite refinement by rapid solidification, thus improving mechanical properties such as friction [4] or fatigue [5] behaviors. LSM is also receiving great attention

among corrosion workers and industrials to improve the localized corrosion resistance of stainless steels. Mudali and Dayal [6–8] reported that intergranular corrosion (IGC) resistance improvements evidenced after LSM could be attributed to the dissolution or redistribution of the carbide precipitates and the homogenization of the Cr-depleted zones. Also, the development of a homogeneous microstructure tends to improve the pitting corrosion resistance because of the elimination of probable pit nucleation sites such as MnS inclusions [7–9]. For Pan *et al.* [10], in addition to the redistribution of carbides, the improvement of IGC resistance on a AISI 321 can also be attributed to the formation of  $\delta$ -ferrite, due to a high  $\text{Cr}_{\text{eq}}/\text{Ni}_{\text{eq}}$  ratio.  $\delta$ -ferrite influences the segregation of Cr, limits the Cr depleted zone and eliminates continuous pathways for IGC. However, Pan reported a deleterious effect of  $\delta$  ferrite on the pitting corrosion, because of the potential difference existing between  $\gamma$ -austenite and  $\delta$ -ferrite. Opposite effects were pointed out by Kwok *et al.* [11] on AISI 304 and 316: due to the trapping of sulfur in the  $\delta$  ferrite and the redistribution or

removal of MnS, some improvements of the pitting resistance are evidenced despite a decrease of the cavitation erosion resistance. Last, Nakao *et al.* [12] have used the LSM on weld zones of Mo-containing austenitic stainless steel to improve the corrosion resistance by homogenizing the Mo and Cr depleted zones.

All the previously related experiments involving corrosion improvements by LSM have been performed with continuous wave (cw) or pulsed CO<sub>2</sub> [5, 7, 9, 10, 12] and YAG [8, 11] lasers.

In the present study, LSM has been carried out on 316L SS using a new generation 1 kW cw high power diode laser (HPDL). This novel laser technology allows to generate high cw powers with lower costs and a much more compact design than conventional sources. Moreover, the laser-material coupling is expected to be improved because of a lower wavelength (0.954 μm) than CO<sub>2</sub> (10.6 μm) or YAG (1.06 μm) sources, driving to enhanced absorptions. Last, the beam shape of diode lasers (rectangular) appears to be appropriate for surface treatment applications [13]. With the use of such HPDL, different surface treatments have already been investigated like transformation hardenings in solid phase on carbon steels [14], or surface melting to improve the wettability characteristics of mild steels [15].

The first part of this work was designed to evaluate the process efficiency by 2D finite element thermal modeling of a 1 kW HPDL surface melting on a hyper-quenched 316L SS.

Thereafter, we aimed to characterize the chemical and microstructural modifications, and to investigate the resulting effects on pitting corrosion resistance, by the use of rest potential recordings and potentiodynamic anodic polarizations in NaCl 0.05 M. Also, multipitting tests were carried out to estimate the statistical effect of LSM.

Last, comparisons are made between LSM effects and those induced by pure mechanical treatments such as laser-peening and shot-peening, already applied on the same steel [16, 17].

## 2. Experimental

### 2.1. Material and specimen preparation

LSM experiments have been performed on an AISI 316L steel with composition given in Table I. The base steel exhibits a hyper-quenched state (1060°C/2 h + water quenching) driving to a single austenite microstructure with 30–70 μm equiaxed grain, resulting in a 320 MPa static Yield strength at 0.2% elongation. The modified Schaeffler diagram [18]: was used to estimate the microstructure of as-melted zones. The chromium equivalent (Cr<sub>eq</sub>) and nickel equivalent (Ni<sub>eq</sub>) were defined as:

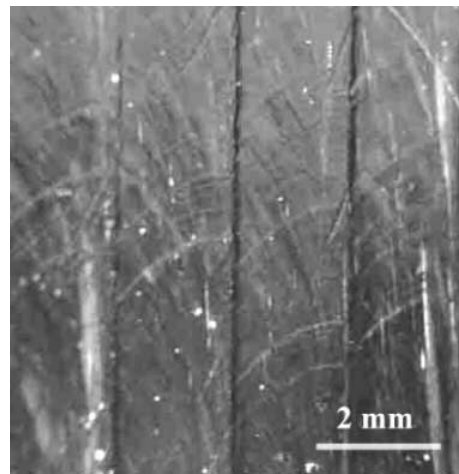


Figure 1 Laser melted paths and solidification lines on the surface.

$$\text{Cr}_{\text{eq}} = [\text{Cr}] + [\text{Mo}] + 1.5[\text{Si}] + 0.5[\text{Nb}]$$

$$\text{Ni}_{\text{eq}} = [\text{Ni}] + 0.5[\text{Mn}] + 30[\text{C}] + 30[\text{N}]$$

With these values, we can estimate a Cr<sub>eq</sub>/Ni<sub>eq</sub> ratio above 1.5, and a 5% δ-ferrite estimated content that tends to drive to a dual solidification mode (ferrite + austenite), with a rather low hot-cracking susceptibility. Quantitative analysis of surface inclusions by X-ray spectrometry indicates mainly the presence of Mn, Ti, Al, Si, Ca, Mg and Cu compounds in the form of aggregates, where all chemical elements are oxidized. Last, the 316L steel contains a very small amount of manganese sulfide, which are the usual active anodic sites for the pit initiation in stainless steel in the presence of chloride.

Before the treatment, the samples (40 × 40 mm) were polished up to 1000 grit SiC paper. After LSM, 12 cylinders of 14 mm diameter were machined by electro-erosion in order to preserve the melted surface. Prior to electrochemical tests, two surface conditions were investigated: (1) the as-melted surface + OPS polishing including a possible oxidized layer, and (2) a 80 ± 30 μm SiC paper + OPS polishing to remove surface waviness due to LSM and ensure a smooth and mirror-like surface. Both conditions differ by their surface aspect (higher roughness for the as-melted surface: Fig. 1) but exhibit nearly the same surface microstructure, except small differences in the primary dendrite arm spacings (DAS) which tend to decrease closer from the surface.

### 2.2. Laser surface melting

Laser melting treatment was carried out using a 1 kW cw diode laser (Rofin Sinar DL015) operating at 0.954 μm wavelength. After focusing on a 80 mm focus length optical lens, the laser beam spot has a 1 × 4 mm rectangular shape, resulting in a maximum intensity of approximately 2.5 × 10<sup>4</sup> W/cm<sup>2</sup>. Helium coaxial shielding at 10 l · min<sup>-1</sup> was used to limit oxidation. Using a scanning speed of 3 mm · sec<sup>-1</sup>, the laser beam passes over the workpiece and produces individual melting paths. A 2 mm lateral step between subsequent laser paths was chosen to obtain an 50% overlap

TABLE I Chemical composition of 316L steel (wt%) determined by Glow Discharge Optical Spectroscopy (GDOS) determination

Fe	Cr	Ni	Mo	C	S	N	Mn
Bal	17.1	11.95	2	0.019	0.007	0.05	1.68

(Fig. 2). The overlap of 16 paths of 4 mm forms the treated sample. With these conditions, each part of the sample is submitted to 2 laser melting events (Fig. 1).

### 2.3. Characterization of metallurgical, mechanical and chemical modifications

The characterization of microstructure and chemical compositions of laser treated surfaces was investigated by optical microscopy (OM), secondary ion mass spectrometry (SIMS) and electron probe microanalysis (EPMA). Vickers hardness measurements were carried out with a 0.05 kg load on the melted surface and on a cross section.

The residual stresses were determined by the X-ray diffraction (XRD) technique using the slopes of the  $2\Theta = f(\sin^2 \psi)$  curves [19] with conditions presented in Table II.

### 2.4. Electrochemical tests

A three electrodes device (Saturated Calomel Electrode SCE as reference electrode, metal surface as working electrode and platinum as counter electrode) controlled by a potentiostat (Solartron SI1287 electrochemical interface) was used for electrochemical testing in NaCl 0.05 M, with a constant regeneration of the solution in the electrochemical cell. Two kinds of tests were displayed on 316L samples. The first one consists of a rest potential recording  $E^0 = f(\text{time})$  during 2 hours, which gives information on the passive film evolution.

The second one is a potentiodynamic test  $I = f(E)$  at 2 mV/sec scan rate to determine the pitting initiation potentials  $E_{gp}$ , (when  $I$  exceeds  $100 \mu\text{A}/\text{cm}^2$ ), the protection values  $E_{pp}$  (during the potential reversal, when  $I$  turns to its initial passive value) and the mass loss during pitting.

Experiments were also carried out on a multipitting device at 2.5 mV/sec to obtain experimental data from up to 12 simultaneous polarizations curves. According

TABLE II XRD Experimental conditions

Anticathode	Filter	Number of $\psi$ angles	{hkl} plans	2 $\theta$ Bragg	E	$\nu$
Mn	Cr	13	{311}	152	195 GPa	1.79

to Shibata [20], a statistical analysis of measurements can be made, driving to a non-survival probability for pits  $\varpi_E$  ( $\text{cm}^{-2}$ ) depending on the pitting probability  $P(\%)$ .

$$\begin{aligned} \varpi_E(\text{cm}^{-2}) &= -\frac{1}{S} \cdot \ln\left(\frac{n - n_E}{n}\right) \\ &= -\frac{1}{S} \cdot \ln\left(1 - \frac{P(\%)}{100}\right) \end{aligned} \quad (1)$$

### 3. Finite element (FE) simulation of diode laser surface melting

The commercial finite element code ABAQUS [21] was used to determine the thermal response of 316L steel to a 1 kW power, resulting in a  $2.5 \times 10^4 \text{ W}/\text{cm}^2$  as the input flux parameter in the \*DFLUX subroutine of the code, corrected by the absorptivity of the steel at  $0.954 \mu\text{m}$  wavelength. The flux distribution on the heated zone was considered to be homogeneous.

4 nodes diffusive-conductive rectangular elements were used to realise a 2D meshing of the irradiated steel. The 1 mm-width moving heat source (3 mm/s) was simulated by the use of a constant calculation step equal to the time increment (0.033 s) between two contiguous surface elements (0.1 mm width). Temperature-dependent thermal properties (conductivity, specific heat) of 316L have been taken from [15] and are reported in Table III.

The aim of the calculation was to optimize the heat input in order to estimate the diode laser absorptivity  $A$  on 316L, and to calculate the thermal history of the metal. For this purpose, 2D analysis of diode melting have been performed with corrected input flux depending on absorption coefficients ( $\phi = 2.5 \times 10^4 \text{ W}/\text{cm}^2 \times A$ ).

TABLE III Temperature-dependent thermal and Physical properties of 316L steel

Temperature ( $^{\circ}\text{C}$ )	Density $\rho$ ( $\text{kg}/\text{m}^3$ )	Conductivity $\lambda$ ( $\text{W}/\text{m}/\text{K}$ )	Specific heat $C_p$ ( $\text{J}/\text{kg}/\text{K}$ )	Latent Heat $\Delta H$ ( $\text{J}/\text{kg}$ )
20	7.96	15.5	452	
400	7.7	20.5	561	
800	7.6	25.1	628	
1000	7.5	27	722	
1200		29	900	$2.7 \times 10^5$
1450				$2.7 \times 10^5$

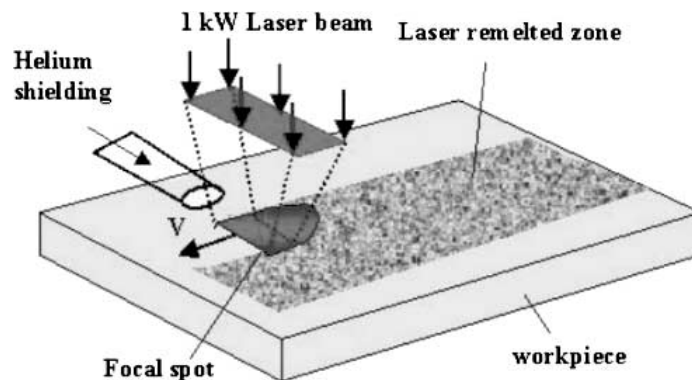
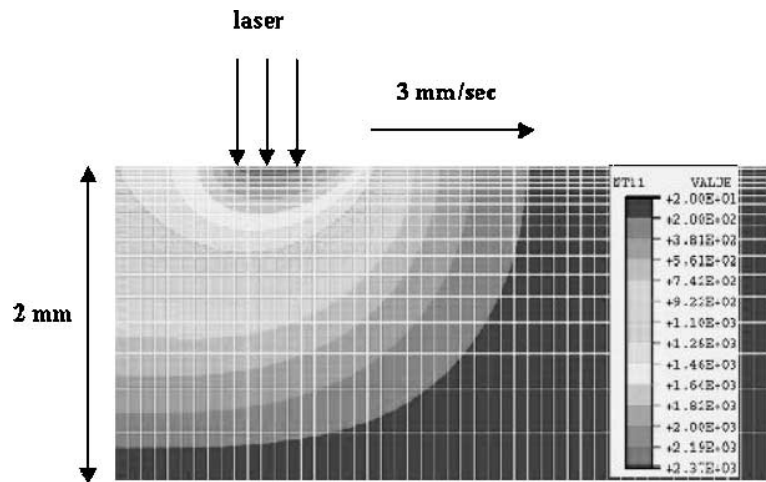
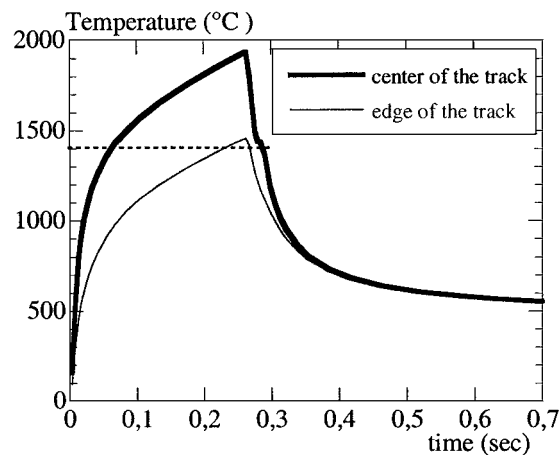


Figure 2 Schematic of a diode laser surface melting (DLSM).



(a)



(b)

Figure 3 Finite element simulation of a DLSM with a  $7 \times 10^3 \text{ W/cm}^2$  flux heat source moving at 3 mm/sec on the surface: (a) isotherms, (b) Thermal history of the surface.

The best correlation between experimental melted zone (fusion isotherm) and simulation was found for  $\phi = 7.10^3 \text{ W/cm}^2$  resulting in  $A \approx 0.28$  absorptivity. The depiction of temperature fields induced by the optimized laser-melting event is given in Fig. 3a. Corresponding Temperature vs. time profiles are given in Fig. 3b. The heating rate can be estimated to  $20000^\circ\text{C/s}$  between ambient temperature and Fusion ( $1410^\circ\text{C}$ ) and the cooling rate to nearly the same value between the maximum temperature in the molten pool ( $1950^\circ\text{C}$ ) and  $700^\circ\text{C}$ . This high cooling rate, which gives an upper value limit of the solidification rate, results in a fine dendritic microstructure ( $\text{DAS} \approx 3 \mu\text{m}$ ), more widely investigated in Section 4.

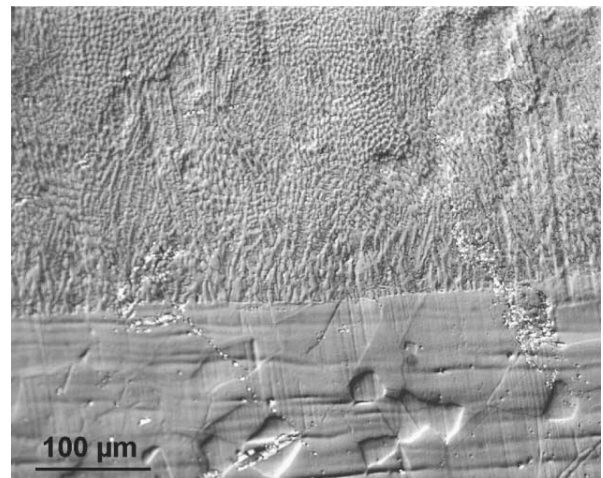


Figure 4 Optical micrograph of a LSM cross-section.

## 4. Experimental results

### 4.1. Characterization of laser melted surface

#### 4.1.1. Microstructure

The cross-sectional microstructure of a specimen (Fig. 4) shows a melted zone constituted by solidification dendrites on a  $400 \pm 50 \mu\text{m}$  depth. The dendritic structure tends to become finer from the boundary between the melted region and the substrate to the surface. This corresponds to a change in the solidification mode from a basaltic (low solidification rate) to an equiaxed

structure (high solidification rate and low thermal gradient). Also, EPMA analysis (Fig. 5) shows a small decrease of Ni content at the border of the melted zone and within the dendrite arm spacings (DAS or interdendritic zones). Thus, nickel content is about 9% in interdendritic zone and 12% in dendrite cores. The same observations could be made for Mn and Si. In contrast, the chromium content follows the opposite

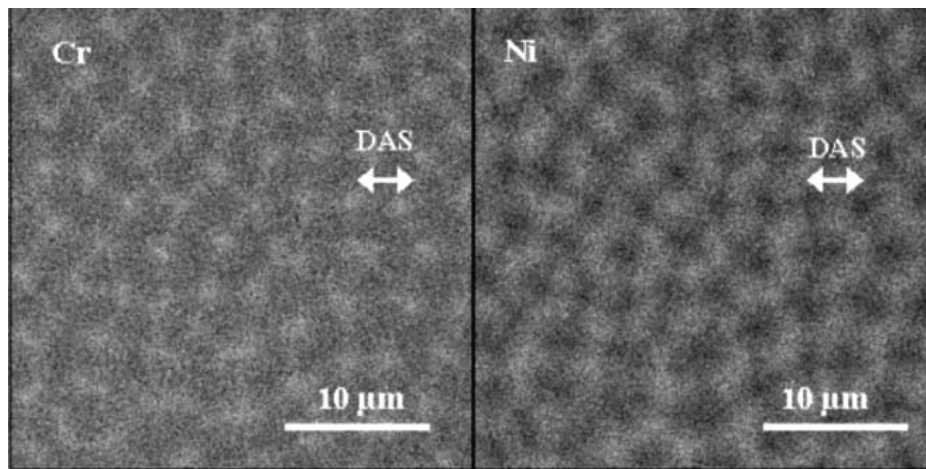


Figure 5 Microsegregation phenomena during laser surface melting (EPMA analysis): Chromium enrichment and Ni depletion in the interdendritic equiaxe solidification zones (dendrite arm spacings DAS = 3 μm).

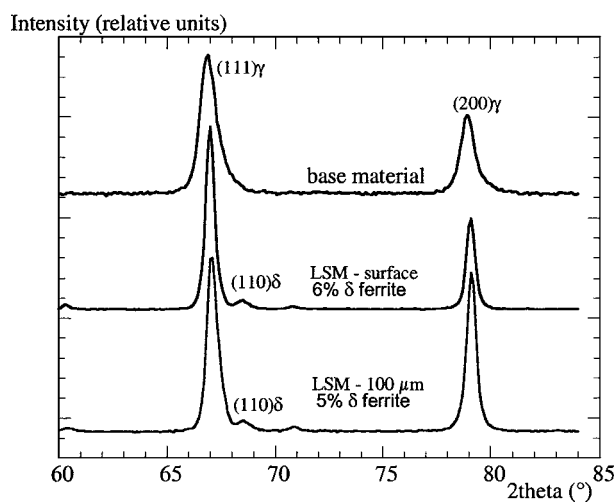


Figure 6 X-ray diffraction on the LSM specimen surface.

evolution: it increases from the middle (16%) to the edge (18%) of the  $\gamma$  dendrites. This reveals a microsegregation of Cr during solidification, with a step-by-step chromium enrichment of the liquid when the solidification front grows from the center to the border of dendrites. DAS tend to decrease on the direction of thermal gradient, from more than 20 μm in basaltic region to 3–5 μm in the upper equiaxe structure.

X-ray diffraction spectra on the surface specimen before and after LSM exhibit  $\delta$ -ferrite peaks in Fig. 6, with a 6% content estimated from the ratio of the integrals of body-centered cubic  $\delta$  peaks and face-centered cubic  $\gamma$  peaks, corrected by different experimental factors, as defined [22]:  $C_{\delta} = (1 + 1.25 * \frac{I_{\gamma}}{I_{\delta}})^{-1}$ . This  $\delta$  content appears to be rather constant on the first 100 μm in-depth, where corrosion behavior has been investigated.

Fig. 7 shows optical micrographs of the melted region at higher magnification. The  $\delta$ -ferrite phase, colored yellow-brown by the Murakami reagent, is present in interdendritic section in the form of skeletal network around austenitic matrix.

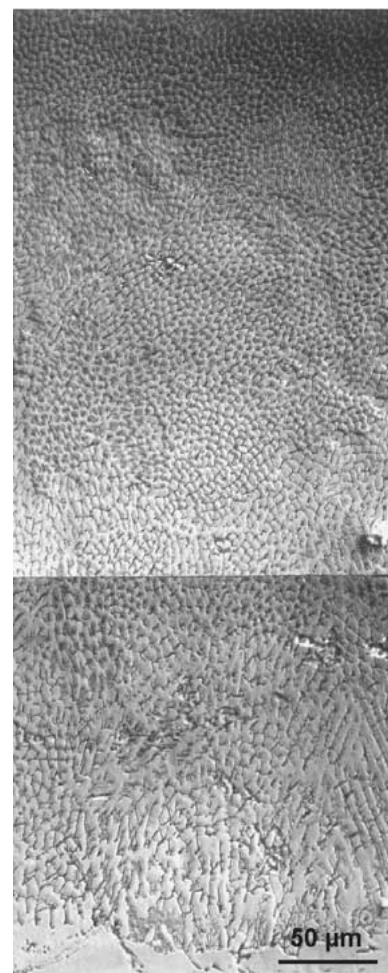


Figure 7 Optical micrograph of a LSM cross section etched by Murakami reagent: equiaxe solidification zone (upper part) and longitudinal zone (lower part). Localization of  $\delta$  ferrite in the interdendritic zones.

#### 4.1.2. Chemical analysis of the surface and the inclusions

SIMS and EPMA analysis confirm that LSM preserve the global chemical composition of base materials, without occurrence of surface pollutions. Nevertheless, the EPMA imaging (Fig. 8) reveals that inclusions in form of aggregates ((Al, Mn, Ti), (Al, Mn, Ti, S), (Al, Ca)) are present only in the substrate, and not any more

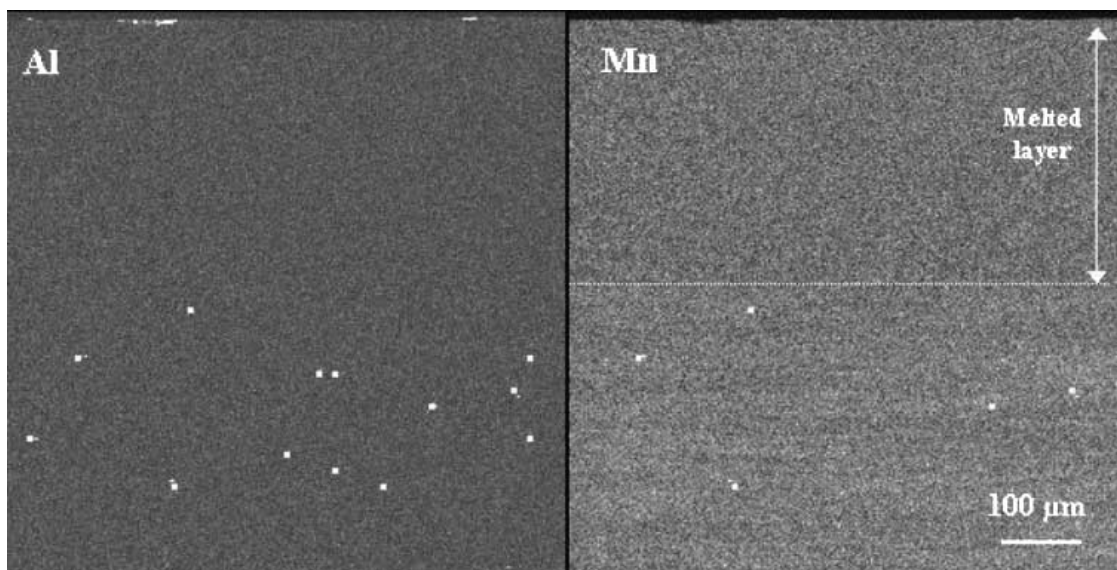


Figure 8 EPMA analysis of inclusions in LSM cross-sections for Al and Mn elements (inclusions luminosities have been emphasized by white points): all inclusions are removed from the laser-melted layers except Si-base aggregates.

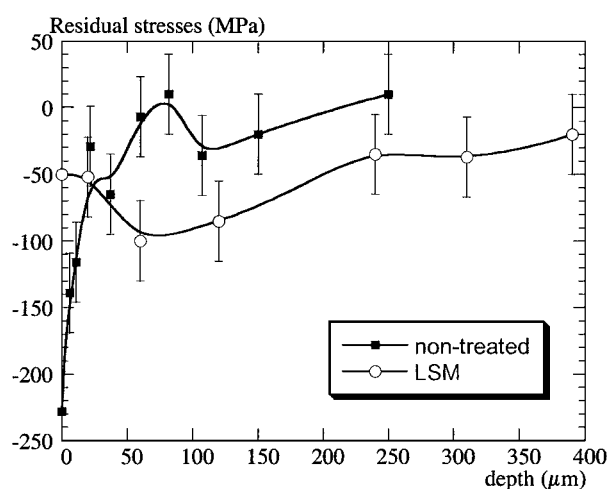


Figure 9 In-depth residual stresses profiles (XRD analysis) on laser melted and as-received material.

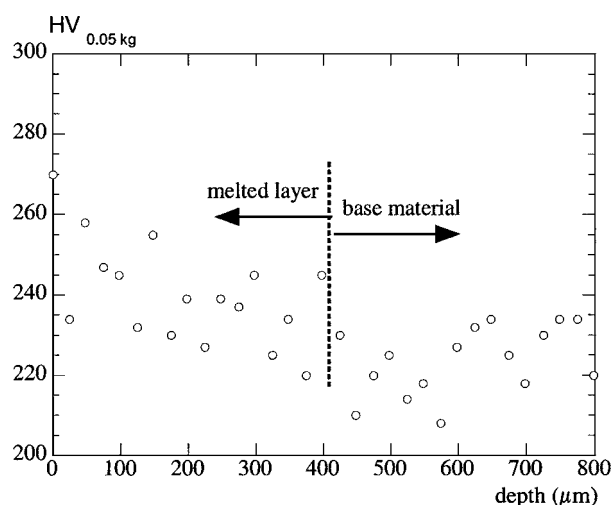


Figure 10 In-depth Vickers hardness profiles on laser melted specimen (50 g loading).

in the LSM zone. These inclusions have been dissolved or redistributed by LSM. Only Si-based inclusions (certainly silicon oxide or silicon carbides) are still present in the melted zone.

#### 4.1.3. Mechanical modifications: residual stresses and microhardness

XRD analyses have been carried out on the melted surface and in-depth. The residual stresses (RS) profiles (Fig. 9) across the melted region reveal that RS are always compressive. RS increase from  $-50 \pm 30$  MPa on the surface to  $-100 \pm 30$  MPa for a  $60 \mu\text{m}$  melted depth. Below this maximum, RS decrease until the boundary between the unmelted substrate and basaltic zone.

During the solidification, as the liquid phase volume tends to shrink, the surrounding substrate is expected to generate tensile stresses to oppose to this restraint. Thus, previous authors have reported a residual tensile state after surface melting [9]. However the plastifica-

tion during cooling and/or the development of  $\delta$ -ferrite, can provoke a decrease of tensile RS and even turn tensile into compressive RS. For instance, Kwok *et al.* [11] reported that stainless steels where  $\delta$ -ferrite was detected, had compressive residual stresses, whereas tensile residual stresses were found for SS without  $\delta$ -ferrite. Besides, even if there was not significant evidence of surface cracking, the presence of small microcracks could explain surface stress relaxation.

The hardness profiles across the cross-section of the melted region is shown in Fig. 10. The hardness values are increased to a slight extent after LSM (+10%), due to the refinement of dendrites, and the presence of  $\delta$  ferrite, which has a higher strength and hardness than austenitic phase. Near the surface, the refinement is more important than near the interface (Fig. 7). Thus, the hardness decrease near the boundary between the LSM region and the as-received steel could be attributed to the increase of DAS and the equiaxe-columnar transition.

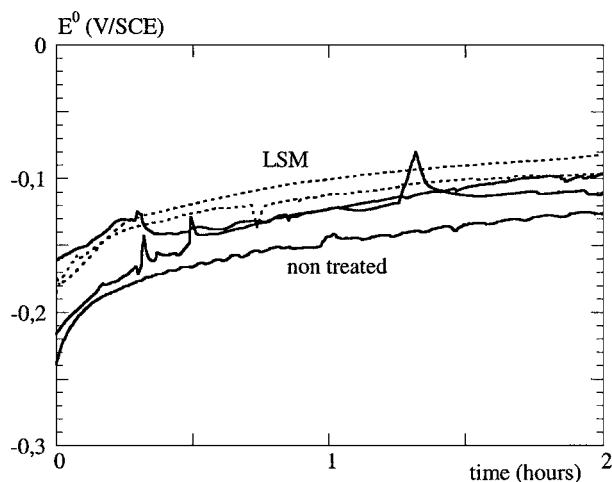


Figure 11 Rest potential  $E^0$  (V/SCE) versus time for melted specimens in NaCl 0.05 M.

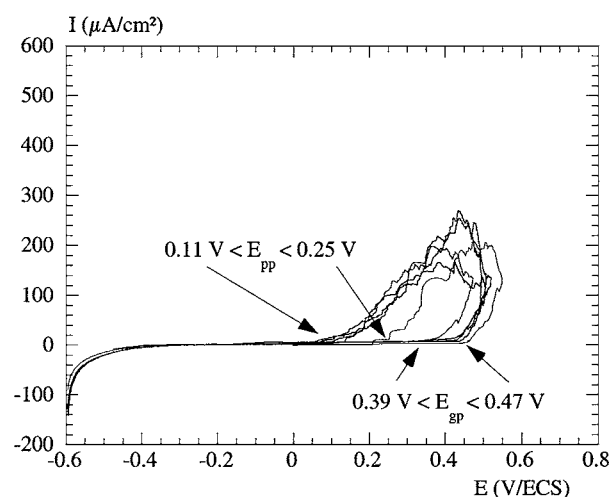


Figure 12 Potentiodynamic polarization curves of as-received 316L steel at 2 mV/sec scan rate in NaCl 0.05 M.

#### 4.2. Electrochemical behavior

The potential versus time curves in Fig. 11 reveal that the rest potential of melted specimen is reproducible and stable enough, except 1 to 2 fluctuations. LSM tends to generate a small anodic shift and in-turn an ennoblement of  $E_{rest}$  after surface treatment when compared to the non-treated 316L. However, after 2 hours recording, potentials become closer and closer indicating similar evolution (growth and ageing) of the passive film. Moreover, no difference could be pointed out between samples polished by OPS only, and those with  $-100 \mu\text{m}$  polishing. So, rest potentials are apparently not influenced by removed thickness, because the surface state is constituted for both by a equiaxed dendritic and microsegregated structure. Cyclic potentiodynamic polarization curves at 2 mV/s of non treated and laser melted surfaces are shown in Figs 12 and 13. From these curves, the following conclusions can be made:

(i) Anodic shifts of  $E_{gp}$  are evidenced after LSM: from  $0.43 \pm 0.04 \text{ V}$  to  $0.62 \pm 0.08 \text{ V}$ .  $E_{gp}$  values appear to be more scattered after LSM treatment.

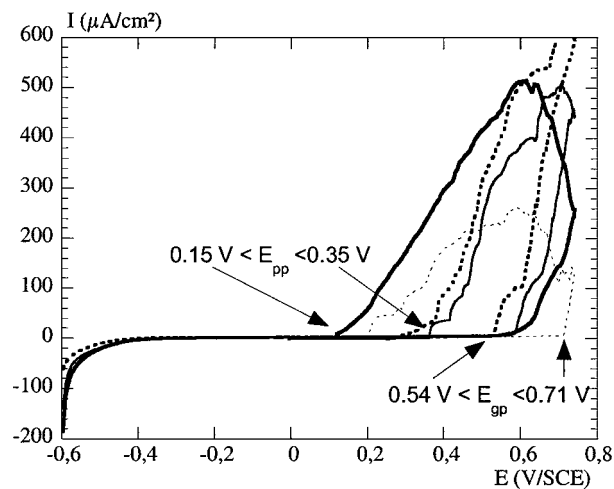


Figure 13 Potentiodynamic polarization curves of laser melted specimen ( $-80 \pm 20 \mu\text{m}$ ) in 0.05 M NaCl solution at 2 mV/sec scan rate.

(ii) Protection potentials  $E_{pp}$  are also increased, but only to a small extent ( $0.18 \pm 0.07 \text{ V}$  to  $0.25 \pm 0.1 \text{ V/SCE}$ ).

(iii) If we compare  $I = f(E)$  curves (for non-treated and LSM samples having nearly the same  $E_{gp}$ ), during the potential reversal driving to the repassivation (between  $E_{gp}$  and  $E_{pp}$ ), the mass loss (calculated from the integral of the  $I = f(t)$  curves) is increased by a factor 2 ( $6 \mu\text{g}$  to  $12 \mu\text{g}$ ). As the number and size of pits is nearly the same on both surface conditions, this may be ascribed to crevice corrosion occurring during potential reversal, only in the case of LSM samples.

(iv) The passive plateau current density (average value between 0.1 and 0.3 V) is lowered from  $5 \pm 2 \mu\text{A/cm}^2$  to  $2 \pm 1 \mu\text{A/cm}^2$  after LSM. This result, which differs from previous investigations [9] indicates a stronger passive film, less prone to damage by chloride ions.

(v) No difference could be evidenced between the two LSM conditions behaviors (after  $-5 \mu\text{m}$  or  $-100 \mu\text{m}$  polishing from the as-melted surface).

Except the occurrence of crevice corrosion, small difference could be pointed out concerning the pitting attack (localisation and size). In NaCl  $-0.05 \text{ M}$  solution, pits before and after LSM are usually small (2 or 3 pits  $> 50 \mu\text{m}$  and many micropits), and randomly localized in the samples (Fig. 14). The only difference may come from the number of pits: more micropits ( $\approx 10\text{--}20 \mu\text{m}$ ) seem to initiate after LSM.

The use of multipitting device on five LSM samples polarised in the same time at 2.5 mV/sec confirm the results obtained at 2 mV/sec (Fig. 15): pitting potentials are shifted towards anodic values by 0.15 to 0.25 V, but results are more scattered after LSM. One should notice that potential values are somewhat higher than those achieved at 2 mV/s because of the higher potential scan rate during multipitting tests. During the same experiments, non-polished LSM samples have been investigated to evaluate the pitting resistance of as-melted specimens. A nearly  $-80 \text{ mV}$  reduction of  $E_{gp}$  was evidenced. Several explanations for this very specific behavior will be discussed in Section 5.

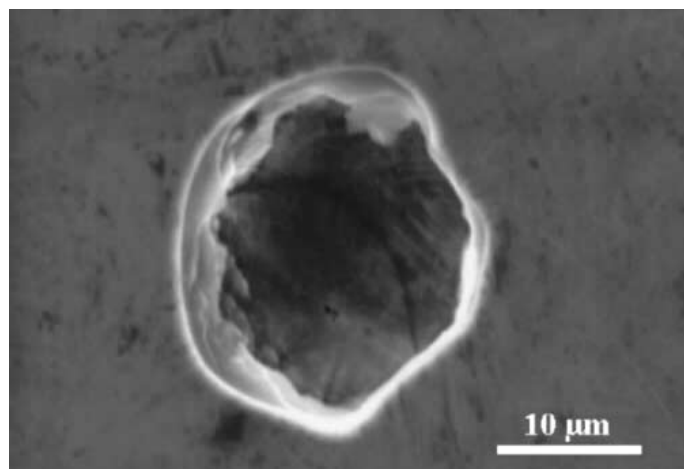


Figure 14 Pits on a LSP + 80  $\mu\text{m}$  polishing surface.

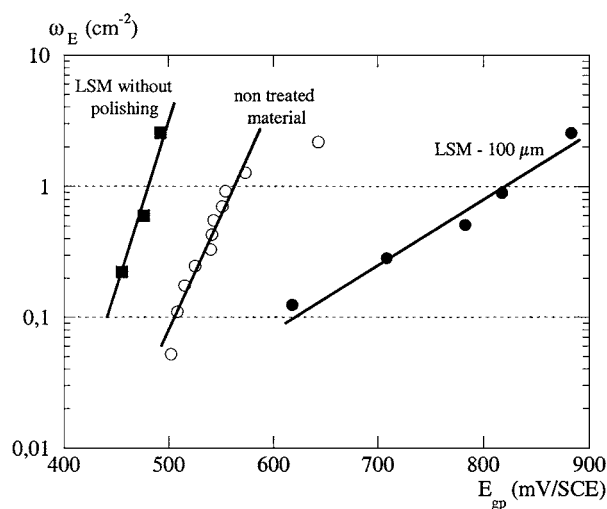


Figure 15 Multipitting experiments at 2.5 mV/sec: Influence of diode Laser surface melting (LSM) on the statistical results of pitting.

## 5. Discussion

Some significant improvements of the pitting corrosion behavior of a non-sensitized 316L steel in NaCl 0.05 M have been evidenced after HPDL surface melting, despite the occurrence of a lower sub-joint crevice resistance, and provided the surface was polished to a mirror-like aspect after LSM. This has been confirmed by potentiodynamic tests at 2 mV/s and 2.5 mV/s. On the other hand, multipitting corrosion tests performed at 2.5 mV/s on as-melted specimens evidenced a low corrosion resistance than base material ( $-80$  mV on Fig. 15).

The depreciation of pitting resistance of as-melted 316L was attributed to many factors: a rougher surface state driving to a bad passive film construction, maybe surface microcracks (non detectable by optical systems) due to local modification of the Cr/Ni content (higher N content for instance due to insufficient He shielding), and also the generation of a very superficial amorphous structure previously mentioned in [9].

The increases in pitting potential evidenced on 316L after laser melting are a little higher (+200 mV) than those from previous studies on 316 or 304 steels [6, 10, 11]. However, the explanations are different. For

Kwok *et al.* [11], more significant improvements are evidenced on 316 stainless steel (SS) than on 304 SS after LSM, due to the removal of MnS inclusions on 316 SS, and to an increase of  $\delta$  ferrite content on 304 SS. The redistribution of inclusions and the homogenization of constitutive elements on a 316L melted zone contribute for Dayal *et al.* [6, 7] to obtain a better passive film, more resistant to localized corrosion attack in  $\text{Cl}^-$  environment.

The redistribution of oxide inclusions (Al, Mn, Ca, and Ti) which are less harmful than MnS inclusions allows eliminating or reducing possible pitting sites on the surface. The remaining inclusions are Si-base particles which melting point is higher than the maximum temperature reached in the fusion zone during LSM ( $\approx 2000^\circ\text{C}$ ). These inclusions, evidenced by EPMA analysis, are expected to be silicates ( $\text{SiO}_3^{2-}$ ) or SiC particles at high dissolution potential where pits can initiate at nearly 0.6 V/SCE. However, we can assume that the occurrence of pits initiation on SiC inclusions is not obvious because of the low carbon content (0.02%) in the base steel. On the other hand, silicon is used during the casting of stainless steels to improve the resistance to hot oxidation. Therefore, silicates are more usual inclusions and, in our case, more probable inclusions for pit initiation.

It has been shown that LSM generates 6%  $\delta$ -ferrite and a refinement of structure that allows to obtain compressive residual stresses and a 10% hardness increase on the melted zone. Previous studies indicate that the  $\delta$ -ferrite surface content is expected to gradually increase in-depth, due to a decrease of the cooling rate towards the boundary with the unmelted specimen. As we only have investigated the first 100  $\mu\text{m}$  in-depth, we could consider as negligible the changes in cooling rate and delta ferrite content.

The influence of cooling rates on the pitting corrosion resistance has already been investigated widely by Pan *et al.* [10] on sensitized 321 structure. With a 200  $\text{kW}/\text{cm}^2$  irradiation and a 50 mm/s to 100 mm/s scanning speed, the authors evidenced a dissolution of grain boundary precipitates and an homogenization of the molybdenum and chromium contents. In any case, significant improvements of the pitting resistance were

pointed out despite some changes in the  $\delta$  volume ratio (possibly detrimental to the pitting behavior because of possible galvanic coupling between  $\delta$  and  $\gamma$  phases). Therefore, the influence of  $\delta$  ferrite content was considered as negligible as compared with other LSM effects.

In our case, on a “non-sensitized” 316L irradiated with a 25 kW/cm<sup>2</sup> power density, a small chromium microsegregation occurred, due to rather low solidification rates compared with usual laser remelting (3 mm/s scanning speed versus 50–100 mm/s). So it can be assumed that the anodic shift of pitting potentials  $E_{gp}$  (0.43 to 0.62 V/SCE) has not been achieved by the homogenization of Cr and Mo contents, but by the simple dissolution of usual sites for pitting (Al and Mn aggregates in the form of oxides).

Concerning the passive behavior, the factor 2 decrease of passive current and the small anodic shift on rest potentials  $E^0$  after LSM, seem to indicate the formation of a more stable passive film, despite local composition gradients due to microsegregations, and  $\delta$  ferrite generation. As surface roughnesses and film aging are the same, it seems that microsegregations do not prevent the passive film structure from being globally more resistant to chloride ions damage. The presence of compressive stresses also may have contributed to the creation of a stronger passive layer. Indeed, comparable enhancements of  $E^0$  and  $E_{gp}$  have been shown recently on the same 316L steel after compressive stress generators treatments such as laser peening or shot-peening [16, 17]. As these treatments preserve the inclusion density, the chemical composition and the surface roughness, the increase of pitting potentials and the improvement of passive behavior was ascribed exclusively to the compressive stress field. Thus, the occurrence of a mechanochemical effect [23] contributing in increased resistance to corrosion can possibly be mentioned to explain the modification of passive behavior.

## 6. Conclusion

Pitting corrosion studies on type 316L stainless steel specimens have shown a significant improvement in pitting corrosion resistance following laser surface melting. From these results, the following conclusions can be made:

(i) The main effect which reduces the corrosion attack after laser surface modification and increase the pitting potential  $E_{gp}$  (+0.2 V) is the development of a finer surface microstructure, in which undesirable precipitates (Al and Mn aggregates) are eliminated or redistributed.

(ii) The passive behavior is improved with a factor 2 decrease of the passive current density, indicating that

chromium microsegregation and 6%  $\delta$  ferrite do not have a detrimental effect on passive film behavior.

(iii) A possible contribution of the compressive stress field generated during LSM was evidenced, driving to a stronger passive film, less prone to damage by chloride ions.

(iv) LSM resulted in a depreciation of crevice corrosion resistance during polarization tests.

## References

1. R. KE and R. ALKIRE, *J. Electrochem. Soc.* **122**(12) (1995) 4056.
2. J. STEWARD and D. E. WILLIAMS, *Corr. Science* **33**(3) (1992) 457.
3. M. A. BAKER and J. E. CASTLE, *ibid.* **33**(8) (1992) 1295.
4. M. CARBUCICCHIO, G. PALOMBARINI, M. RATEO and G. SAMBOGNA, *Hyperfine Interactions* **112** (1998) 19.
5. H. STAMM, U. HOLZWARATH, D. J. BOERMAN, F. DOS SANTOS MARQUES, A. OLCINI and R. ZAUSCH, *Fat. Fract. Engng. Mater. Struct. Interactions* **19**(8) (1996) 985.
6. K. MUDALI, R. DAYAL, J. GNAMOORTHY, S. KANETKAR and S. OGALE, *Materials Transactions, JIM* **33**(9) (1991) 845.
7. R. DAYAL, *Surface Engineering* **13**(4) (1997) 299.
8. K. MUDALI, R. DAYAL and G. GOSWAMI, *Anticorrosion Meth. & Mat.* **45**(3) (1998) 181.
9. K. MUDALI, M. PUJAR and R. DAYAL, *JMEPEG* **7**(2) (1998) 212.
10. Q. PAN, W. HANG, R. SONG, Y. ZHOU and G. ZHANG, *Surface & Coating Technology* **102** (1998) 245.
11. C. KWOK, H. MAN and F. CHENG, *ibid.* **99** (1998) 295.
12. Y. NAKAO, K. NISHIMOTO and W. ZHANG, *Transactions of the Japan Welding Society* **241**(1) (1993).
13. F. KLOCKE, A. DEMMER and A. ZABOLICKI, *Lasers In Materials Processing*, SPIE Conference, Vol. 3097, edited by L. Beckmann (1997) p. 592.
14. J. LAWRENCE and J. LI, *J. Phys. D: Appl. Phys* **32** (1999) 2311.
15. *Les aciers inoxydables*, Les éditions de Physique (Fr), edited by G. Béranger and B. Baroux (1990).
16. P. PEYRE, X. SCHERPEREEL, L. BERTHE, C. CARBONI, R. FABBRO, G. BÉRANGER and C. LEMAITRE, *Materials Sciences and Engineering A* **280** (2000) p. 294.
17. C. CARBONI, P. PEYRE, M. FREGONESE, H. MAZILLE, G. BÉRANGER and C. LEMAITRE, in “Surface Modifications Technologies XIV,” edited by T. Sudarshan and M. Jeandin, to be published.
18. A. L. SCHAEFFLER, *Met. Prog.* **56** (1949) 680.
19. G. MAEDER, *Materiaux Techniques (Fr)* **5** (1988).
20. T. SHIBATA and T. TAKEYAMA, *Corrosion N. A. C. E.* **33**(7) (1977) 243.
21. ABAQUS Standard 5.7 software, Hibbit, Karlsson and Sorensen Ed, 1995.
22. B. CULLITY, “Elements of X-ray diffraction” (Addison Wesley, New York, 1978) p. 411.
23. E. M. GUTMAN, “Mechanochemistry of Solid Surfaces” (Ed. World Scientific Publishing, 1994).

Received 29 May 2001

and accepted 27 March 2002